IEEE Access
Multidisciplinary : Rapid Review : Open Access Journal

Received 13 August 2026, accepted 30 August 2026, date of publication 7 September 2026, date of current version 11 September 2026.

Digital Object Identifier 10.1109/ACCESS.2026.3731310

RESEARCH ARTICLE

Control-Oriented Voltage and Current Estimation of Dual Three-Phase PMSMs Considering Spatial Harmonics and Inter-Set Magnetic Coupling

YE-NA BAE[1], HYUN-JEONG HONG[1], JUN-YEOL RYU[1,2], MYUNG-HWAN YOON[3], AND MYUNG-SEOP LIM[1], (Senior Member, IEEE)
[1]Department of Automotive Engineering, Hanyang University, Seoul 04763, South Korea
[2]Korea Automotive Technology Institute, Cheonan 31214, South Korea
[3]Korea Electronics Technology Institute (KETI), Bucheon 14502, South Korea

Corresponding author: Myung-Seop Lim (myungseop@hanyang.ac.kr)

This work was supported by the National Research Foundation of Korea (NRF) grant funded by the Ministry of Science and ICT (MSIT), Republic of Korea, under Grant RS-2026-25496066.

ABSTRACT This paper investigates the effects of rotor-position-dependent spatial harmonics on voltage and current prediction in dual three-phase permanent-magnet synchronous motors (PMSMs) under two current-control strategies. A simplified machine model retains the operating-point-dependent magnetic-saturation state and average inter-set coupling but neglects the spatial harmonics of the inductance and permanent-magnet flux linkage. Analysis of the voltage equations shows that parameter averaging removes nonfundamental voltage components arising from the rotor-position-dependent inductance and PM flux-linkage variations. Under two individual current control, these omitted voltage components excite harmonic currents in both winding sets, causing substantial current-harmonic prediction errors. Under vector space decomposition (VSD) current control, the dominant harmonic currents are actively suppressed in the *DZQZ* subspace, and omission of the same voltage sources instead leads to underestimation of the harmonic controller-voltage demand. To isolate the effects of spatial harmonics, the simplified and detailed models are constructed from identical finite-element-analysis-based parameters obtained using the frozen-permeability method. Simulation and experiments using a prototype dual three-phase PMSM show that the simplified model substantially underestimates the dominant current harmonics under two individual current control and the harmonic voltage demand under VSD current control. These results demonstrate that the prediction limitations caused by spatial-harmonic omission depend strongly on the applied current-control strategy.

INDEX TERMS Dual three-phase, permanent magnet synchronous motor (PMSM), two individual control, vector space decomposition (VSD), spatial harmonics, inter-set coupling.

I. INTRODUCTION

Dual three-phase permanent-magnet synchronous motors (DTP-PMSMs) employ two isolated three-phase winding sets supplied by independent voltage-source inverters. Compared with conventional three-phase machines, they offer reduced phase-current ratings [1], enhanced fault tolerance, and improved system reliability [2], making them attractive for high-power and safety-critical propulsion systems [3], [4], [5]. In asymmetrical DTP-PMSMs, the winding sets are typically displaced by 30° electrical to suppress specific magnetomotive-force harmonics [6], [7]. Although the two sets are electrically isolated, they share the same magnetic circuit. Consequently, the current in one set affects the flux linkage and voltage of the other through inter-set magnetic coupling, which can increase voltage and current distortion and degrade drive-system performance [8], [9].

Simplified machine models based on rotor-position-averaged inductance and permanent-magnet (PM) flux-linkage parameters are widely used because of their simple

The associate editor coordinating the review of this manuscript and approving it for publication was Jinquan Xu.

structure and low computational burden [10], [11]. They are particularly useful for preliminary motor design, controller development, and system-level simulation. By retaining the dc components of the inductance and PM flux linkage, these models can represent the operating-point-dependent effects of magnetic saturation and average inter-set coupling. However, parameter averaging removes the rotor-position-dependent spatial harmonics and their associated nonfundamental voltage-source terms. This omission can cause errors in predicting both current harmonics and the harmonic voltage demand, defined as the nonfundamental controller voltage required for current-harmonic suppression.

To improve prediction fidelity, FEA-based flux-linkage and inductance models have been developed for conventional three-phase PMSMs by accounting for magnetic saturation, spatial harmonics, and iron-loss effects [12]. These approaches have been extended to DTP-PMSMs through multidimensional flux maps and nonlinear current- or flux-based formulations that additionally account for cross-saturation and inter-set magnetic coupling [13], [14], [15]. Subspace decomposition, reduced-dimensional look-up tables, and partial linearization have also been introduced to reduce the associated computational and memory requirements [16]. These studies have primarily aimed to reproduce nonlinear and rotor-position-dependent electromagnetic behavior with improved accuracy and computational efficiency.

Spatial-harmonic-aware models have also been applied to control and motor design. A design-oriented study quantified the harmonic voltage demand under vector space decomposition (VSD) control and incorporated it into geometry design to improve voltage utilization [17]. Model-free and observer-based predictive current-control methods have instead mitigated modeling errors by estimating or compensating for lumped disturbances [18], [19]. These studies demonstrate the practical importance of spatial-harmonic effects or improve robustness against them, but they either retain or compensate for the resulting disturbances without explicitly identifying the individual voltage-source terms removed by parameter averaging.

The unresolved issue is not simply whether retaining spatial harmonics improves prediction accuracy, but how their omission affects different current-control strategies. Under two individual current control, the omitted nonfundamental voltage components primarily appear as current-harmonic prediction errors, whereas under VSD current control, suppression of the corresponding *DZQZ* currents shifts their effect to harmonic controller-voltage demand. Rather than proposing another high-fidelity machine model, this study uses a detailed model as a reference to identify the voltage-source terms omitted by the simplified model and to clarify the resulting control-dependent error mechanisms.

To clarify this control-dependent mechanism, this paper compares simplified and detailed models constructed from identical finite-element analysis (FEA)-based parameters obtained at the same operating point and frozen-permeability state. The models differ only in whether the rotor-position-dependent spatial harmonics are retained, thereby isolating the effect of spatial-harmonic omission.

The main contributions of this paper are as follows:

- The nonfundamental voltage-source terms generated by rotor-position-dependent inductance and PM flux-linkage harmonics, but omitted by the simplified model, are mathematically identified.
- The control-dependent mechanisms by which these omitted terms produce current-harmonic errors under two individual current control and harmonic-voltage-demand errors under VSD current control are analytically clarified.
- The resulting prediction errors are quantitatively evaluated through simulation and experiments using a prototype DTP-PMSM.

The remainder of this paper is organized as follows. Section II presents the FEA- and frozen-permeability-based parameter-extraction method. Sections III and IV analyze the limitations of the simplified model under two individual current control and VSD current control, respectively. Section V presents the experimental validation, and Section VI concludes the paper.

II. INDUCTANCE AND PM FLUX-LINKAGE MODELS CONSIDERING MAGNETIC SATURATION, SPATIAL HARMONICS, AND INTER-SET COUPLING

This section presents the mathematical models and FEA-based extraction procedure for the inductance and permanent-magnet (PM) flux-linkage parameters used in the subsequent analyses. To clarify the physical effects represented by these parameters, magnetic saturation, spatial harmonics, and inter-set magnetic coupling are distinguished according to their respective roles.

Magnetic saturation determines the operating-point-dependent permeability distribution established by the applied currents. Within the resulting magnetic state, spatial harmonics describe the rotor-position-dependent variations of the inductance and PM flux linkage caused by slotting, winding and PM magnetomotive-force distributions, air-gap permeance variation, and local saturation. Inter-set magnetic coupling describes the influence of the current in one winding set on the flux linkage and voltage equation of the other set.

Based on these distinctions, two parameter models are defined using the same FEA-extracted data. The detailed model retains the complete rotor-position-dependent inductance and PM flux-linkage waveforms, whereas the simplified model uses only their rotor-position-averaged components. Because both models are derived from the same operating-point-dependent permeability distribution, they preserve the same magnetic-saturation state and average inter-set coupling. Their only difference is therefore whether the rotor-position-dependent spatial harmonics are retained.

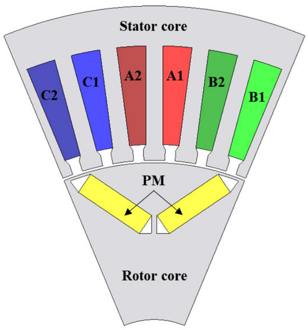

FIGURE 1. Cross section of the 8-pole/48-slot DTP-IPMSM base model.

TABLE 1. Specifications of the motor.

Item	Unit	Value
Poles / slots	–	8 / 48
Winding-set displacement	°	30
Stator diameter	mm	150
Stack length	mm	75
Air-gap length	mm	0.5
Fill factor	%	40
Phase resistance	Ω	0.075
Core material	–	50PN470
Residual induction at 100 °C	T	1.2
DC-link voltage	V	200
Switching frequency	kHz	10

A. FEA MODEL AND NUMERICAL CONDITIONS

The base machine used for the parameter extraction is shown in Fig. 1, and its specifications are listed in Table 1.

A two-dimensional magnetostatic FEA model was used for the nonlinear loaded and frozen-permeability analyses. The nonlinear magnetic properties of 50PN470 electrical steel were defined using the manufacturer-provided *B–H* data. The nonlinear solution was obtained using the Newton–Raphson method with a maximum of 15 iterations and a convergence tolerance of 10^{-3}.

The air-gap region was divided into three radial layers and 180 equal circumferential divisions over half a mechanical pole pitch. The maximum element size in the air-gap and iron-core regions was 0.5 mm.

One electrical period was sampled using 181 rotor positions, including coincident endpoints. This provides 180 intervals of 2° electrical, corresponding to 0.5° mechanical.

B. FROZEN-PERMEABILITY-BASED PARAMETER EXTRACTION

For each operating point defined by the current magnitude I_s and phase angle β, the extraction procedure shown in Fig. 2 was performed over one electrical period to obtain the rotor-position-dependent parameter waveforms:

1) A nonlinear loaded analysis was performed over one electrical period by applying balanced sinusoidal currents to both winding sets with their 30° electrical displacement.

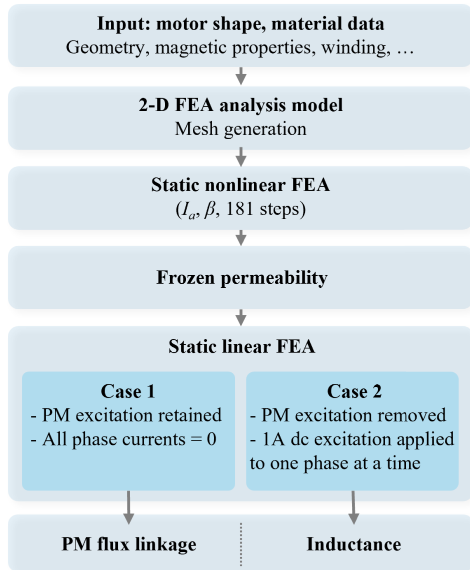

FIGURE 2. FEA-based extraction procedure for the inductance and PM flux linkage under the frozen-permeability condition.

2) The resulting elementwise permeability distribution was frozen at each analyzed rotor position.
3) The phase-domain PM flux-linkage waveform $\boldsymbol{\psi}_{abc}(\theta)$ was extracted with all phase currents set to zero while retaining the PM excitation.
4) The PM regions were replaced by air, and a 1-A dc current was sequentially applied to each phase while the other phase currents were set to zero. The frozen permeability distributions were retained throughout the inductance extraction.

Because the relative permeability of the PM material is close to unity, replacing the PM regions with air removes the remanent-magnetization source with only a negligible change in magnetic reluctance.

Let

$$\mathcal{P} = \{a_1, b_1, c_1, a_2, b_2, c_2\} \tag{1}$$

denote the set of six phases. When phase $k \in \mathcal{P}$ is excited, the inductance between phases j and k is obtained as

$$L_{jk}(\theta) = \frac{\lambda_j^{(k)}(\theta)}{I_{\mathrm{DC}}}, \qquad I_{\mathrm{DC}} = 1\ \mathrm{A}, \tag{2}$$

where $\lambda_j^{(k)}(\theta)$ is the flux linkage of phase j produced by the dc current applied to phase k. Repeating the excitation for all six phases yields the complete phase-domain inductance matrix

$$\mathbf{L}_{abc}(\theta) = \left[L_{jk}(\theta)\right]_{j,k\in\mathcal{P}} \in \mathbb{R}^{6\times 6}. \tag{3}$$

Thus, six excitation analyses provide all self- and mutual-inductance components at each rotor position. Representative phase-domain inductance and PM flux-linkage waveforms are shown in Fig. 3. Owing to phase symmetry, only the parameters associated with phase a_1 are presented.

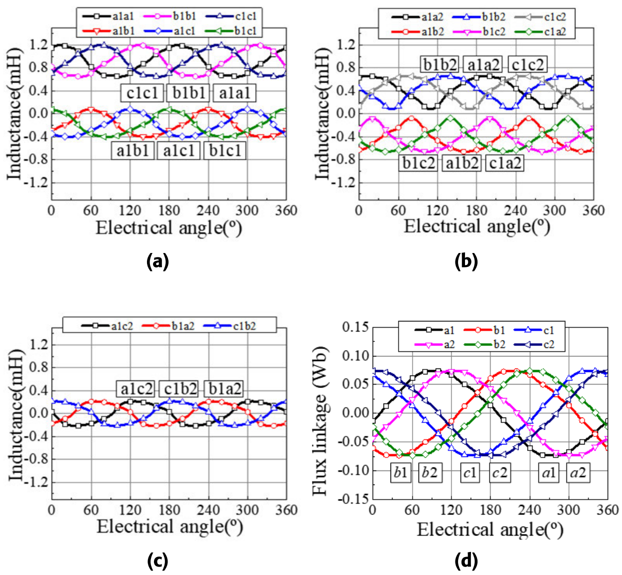

FIGURE 3. FEA-based phase-domain parameters. (a) Self- and mutual inductances with 120° phase displacement. (b) Mutual inductances with 30° and 150° phase displacement. (c) Mutual inductance with 90° phase displacement. (d) PM flux linkage.

C. SPATIAL-HARMONIC REPRESENTATION AND LUT IMPLEMENTATION

For the considered winding configuration, the phase-domain PM flux linkage is represented as

$$\psi_p(\theta) = \sum_{h=1,3,5,\ldots} \psi_p^h \sin\left(h\theta + \alpha_p^h\right), \qquad p \in \mathcal{P}, \tag{4}$$

where ψ_p^h and α_p^h denote the amplitude and phase angle of the hth PM flux-linkage harmonic of phase p, respectively.

The inductance components associated with phase a_1 are represented as

$$L_\kappa(\theta) = L_\kappa^0 + \sum_{h\in\mathcal{H}_\kappa} L_\kappa^h \sin\left(h\theta + \alpha_\kappa^h\right), \tag{5}$$

where κ classifies the inductance component according to the electrical phase displacement between the corresponding windings. Here, L_κ^0, L_κ^h, and α_κ^h denote the dc component, harmonic amplitude, and phase angle, respectively. The component indices are defined as

$$\kappa \in \left\{s,\ 120^\circ,\ 30^\circ,\ 150^\circ,\ 90^\circ\right\}, \tag{6}$$

corresponding to $L_{a_1a_1}$, $L_{a_1b_1}$, $L_{a_1a_2}$, $L_{a_1b_2}$, and $L_{a_1c_2}$, respectively.

The corresponding harmonic-order sets are

$$\begin{aligned}\mathcal{H}_s = \mathcal{H}_{120^\circ} = \mathcal{H}_{30^\circ} = \mathcal{H}_{150^\circ} &= \{2, 4, 6, \ldots\},\\ \mathcal{H}_{90^\circ} &= \{2, 6, 10, \ldots\}.\end{aligned} \tag{7}$$

For the mutual-inductance component with a 90° phase displacement,

$$L_{90^\circ}^0 = 0. \tag{8}$$

The harmonic representations in (4)–(7) are introduced only to describe the parameter variations mathematically and to support the analytical derivations in Sections III and IV. In the time-domain simulations, the detailed model directly uses the FEA-extracted rotor-position-dependent parameter waveforms through periodic one-dimensional look-up tables (LUTs) with linear interpolation, whereas the simplified model uses their rotor-position-averaged components.

Because the objective of this study is to analyze the control-dependent effects of spatial harmonics rather than to implement the model in a real-time controller, this one-dimensional LUT representation is sufficient and introduces only a modest computational burden. No explicit harmonic truncation is applied in the simulations because the sampled parameter waveforms are used directly. The 181 rotor-position samples provide 180 intervals over one electrical period, with a resolution sufficient to represent the dominant sixth- and twelfth-order harmonics considered in this study.

III. CURRENT-HARMONIC PREDICTION ERRORS UNDER TWO INDIVIDUAL CURRENT CONTROL

This section identifies the spatial-harmonic voltage sources omitted by the simplified model and explains how their omission causes current-harmonic prediction errors under two individual current control.

A. COORDINATE TRANSFORMATION AND VOLTAGE EQUATION

The six phase variables are transformed into two individual synchronous dq reference frames using the amplitude-invariant Park transformation:

$$\mathbf{x}_{dq,12} = \mathbf{T}_\mathrm{P}(\theta)\mathbf{x}_{abc,12}, \tag{9}$$

where

$$\begin{aligned}\mathbf{x}_{dq,12} &= \left(x_{d1}\ x_{q1}\ x_{d2}\ x_{q2}\right)^T,\\ \mathbf{x}_{abc,12} &= \left(x_{a1}\ x_{b1}\ x_{c1}\ x_{a2}\ x_{b2}\ x_{c2}\right)^T.\end{aligned} \tag{10}$$

Here, θ denotes the electrical rotor position. The transformation matrices are provided in the Appendix.

Let i denote the winding set under consideration and j the other set, where $i, j \in \{1, 2\}$ and $i \neq j$. The voltage of winding set i is decomposed into self-related and inter-set coupling components as

$$\mathbf{v}_i = \mathbf{v}_i^s + \mathbf{v}_i^c, \tag{11}$$

where $\mathbf{v}_i^s$ is associated with the current and PM flux linkage of winding set i, and $\mathbf{v}_i^c$ is induced by the current of winding set j.

The self-related voltage component is

$$\begin{aligned}\begin{pmatrix} v_{di}^s \\ v_{qi}^s \end{pmatrix} &= R_s \begin{pmatrix} i_{di} \\ i_{qi} \end{pmatrix} + \frac{d}{dt}\begin{pmatrix} L_{di}i_{di} + \psi_{di} \\ L_{qi}i_{qi} + \psi_{qi} \end{pmatrix}\\ &\quad + \omega_e \begin{pmatrix} -L_{qi}i_{qi} - \psi_{qi} \\ L_{di}i_{di} + \psi_{di} \end{pmatrix},\end{aligned} \tag{12}$$

where R_s is the phase resistance, ω_e is the electrical angular speed, L_{di} and L_{qi} are the self-inductances, and ψ_{di} and ψ_{qi} are the PM flux linkages.

The inter-set coupling voltage is

$$\begin{pmatrix} v_{di}^c \\ v_{qi}^c \end{pmatrix} = \frac{d}{dt}\begin{pmatrix} M_d i_{dj} \\ M_q i_{qj} \end{pmatrix} + \omega_e \begin{pmatrix} -M_q i_{qj} \\ M_d i_{dj} \end{pmatrix}, \tag{13}$$

where M_d and M_q are the inter-set mutual inductances.

Expanding (12) and (13) gives

$$\begin{aligned} v_{di} &= R_s i_{di} + L_{di}\frac{di_{di}}{dt} + M_d\frac{di_{dj}}{dt} + e_{di}, \\ v_{qi} &= R_s i_{qi} + L_{qi}\frac{di_{qi}}{dt} + M_q\frac{di_{qj}}{dt} + e_{qi}, \end{aligned} \tag{14}$$

where e_{di} and e_{qi} collect the induced-voltage terms excluding the current derivatives.

B. SIMPLIFIED MODEL

Based on the amplitude-invariant Park transformation in the Appendix, the averaged PM flux linkages are

$$\begin{aligned} \psi_{di}^0 &= \psi_{a_1}^1 \sin\left(\alpha_{a_1}^1\right), \\ \psi_{qi}^0 &= -\psi_{a_1}^1 \cos\left(\alpha_{a_1}^1\right), \end{aligned} \tag{15}$$

where $\psi_{a_1}^1$ and $\alpha_{a_1}^1$ are the amplitude and phase angle of the fundamental PM flux-linkage component of phase a_1, respectively.

The averaged self-inductances derived from (5) are

$$\begin{aligned} L_{di}^0 &= L_s^0 - L_{120^\circ}^0 + \frac{1}{2}L_s^2 \sin\left(\alpha_s^2\right) \\ &\quad + L_{120^\circ}^2 \cos\left(\alpha_{120^\circ}^2 + \frac{\pi}{6}\right), \\ L_{qi}^0 &= L_s^0 - L_{120^\circ}^0 - \frac{1}{2}L_s^2 \sin\left(\alpha_s^2\right) \\ &\quad - L_{120^\circ}^2 \cos\left(\alpha_{120^\circ}^2 + \frac{\pi}{6}\right). \end{aligned} \tag{16}$$

The winding-set displacement is

$$\delta = -\frac{\pi}{6}. \tag{17}$$

For compact notation, define M^0 and M^2 as the dc contributions in the synchronous dq frame originating from the phase-domain zeroth- and second-order components, respectively:

$$\begin{aligned} M^0 &= L_{30^\circ}^0 \cos\delta - L_{150^\circ}^0 \sin\left(\delta + \frac{\pi}{6}\right) \\ &\quad + L_{90^\circ}^0 \sin\left(\delta - \frac{\pi}{6}\right), \\ M^2 &= \frac{1}{2}L_{30^\circ}^2 \sin\left(\delta + \alpha_{30^\circ}^2\right) \\ &\quad + \frac{1}{2}L_{150^\circ}^2 \sin\left(\delta + \alpha_{150^\circ}^2 + \frac{2\pi}{3}\right) \\ &\quad + \frac{1}{2}L_{90^\circ}^2 \sin\left(\delta + \alpha_{90^\circ}^2 - \frac{2\pi}{3}\right). \end{aligned} \tag{18}$$

The averaged coupling inductances are therefore

$$M_d^0 = M^0 + M^2, \qquad M_q^0 = M^0 - M^2. \tag{19}$$

Because the retained parameters are constant in the synchronous reference frames, their derivatives vanish. The induced-voltage terms become

$$\begin{aligned} e_{di}^{\text{simp}} &= -\omega_e\left(L_{qi}^0 i_{qi} + M_q^0 i_{qj} + \psi_{qi}^0\right), \\ e_{qi}^{\text{simp}} &= \omega_e\left(L_{di}^0 i_{di} + M_d^0 i_{dj} + \psi_{di}^0\right). \end{aligned} \tag{20}$$

Thus, the simplified model retains only the speed-induced voltages associated with the averaged self-inductances, coupling inductances, and PM flux linkages.

C. SPATIAL-HARMONIC VOLTAGE SOURCES RETAINED IN THE DETAILED MODEL

The detailed model retains the rotor-position-dependent FEA parameters. As shown in Fig. 4, the self-inductances and PM flux linkages contain dominant $6k$-order components, whereas the inter-set coupling inductances contain dominant $12k$-order components.

These parameters are expressed as

$$\begin{aligned} L_{d,q}(\theta) &= L_{d,q}^0 + \sum_{k=1}^{\infty} L_{d,q}^{6k} \sin\left(6k\theta + \alpha_{L,d,q}^{6k}\right), \\ M_{d,q}(\theta) &= M_{d,q}^0 + \sum_{k=1}^{\infty} M_{d,q}^{12k} \sin\left(12k\theta + \alpha_{M,d,q}^{12k}\right), \\ \psi_{d,q}(\theta) &= \psi_{d,q}^0 + \sum_{k=1}^{\infty} \psi_{d,q}^{6k} \sin\left(6k\theta + \alpha_{\psi,d,q}^{6k}\right). \end{aligned} \tag{21}$$

The compact subscripts d, q denote separate expressions for the two axes, and the superscript 0 denotes the averaged component.

Because θ varies with time,

$$\frac{dx(\theta)}{dt} = \omega_e\frac{\partial x(\theta)}{\partial\theta}, \qquad x \in \left\{L_d, L_q, M_d, M_q, \psi_d, \psi_q\right\}. \tag{22}$$

Differentiation changes the amplitudes and phases but preserves the harmonic orders. Therefore, the $6k$-order self-inductance and PM flux-linkage components generate $6k$-order voltages, whereas the $12k$-order coupling-inductance components generate $12k$-order voltages.

The detailed induced-voltage terms are

$$\begin{aligned} e_{di}^{\text{det}} &= i_{di}\frac{dL_{di}}{dt} + i_{dj}\frac{dM_d}{dt} + \frac{d\psi_{di}}{dt} - \omega_e\left(L_{qi}i_{qi} + M_q i_{qj} + \psi_{qi}\right), \\ e_{qi}^{\text{det}} &= i_{qi}\frac{dL_{qi}}{dt} + i_{qj}\frac{dM_q}{dt} + \frac{d\psi_{qi}}{dt} + \omega_e\left(L_{di}i_{di} + M_d i_{dj} + \psi_{di}\right). \end{aligned} \tag{23}$$

Unlike (20), (23) retains both the parameter-derivative terms and the harmonic components of the speed-induced voltages. Fig. 5 shows the resulting $6k$- and $12k$-order induced-voltage components, which constitute the harmonic excitation omitted by the simplified model.

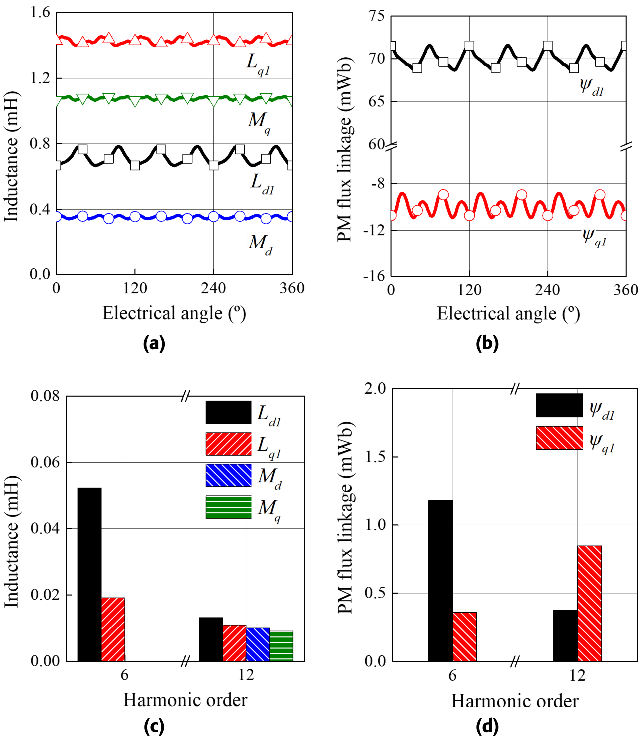

FIGURE 4. Rotor-position-dependent parameters under two individual current control. (a) Inductance waveforms. (b) PM flux-linkage waveforms. (c) Inductance harmonic spectra. (d) PM flux-linkage harmonic spectra.

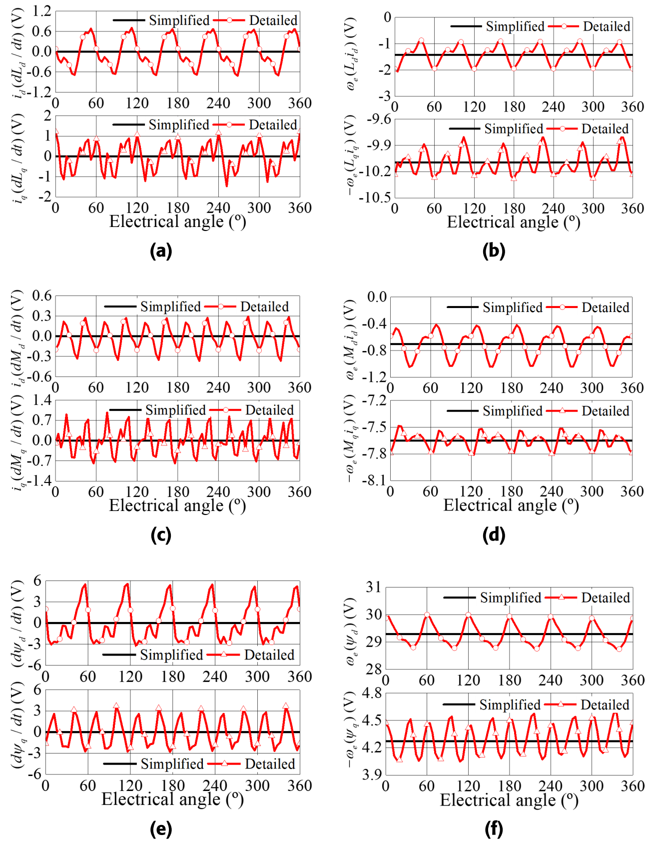

FIGURE 5. Induced-voltage components under two individual current control. (a) $i_{di} dL_{di}/dt$ and $i_{qi} dL_{qi}/dt$. (b) $\omega_e L_{di} i_{di}$ and $-\omega_e L_{qi} i_{qi}$. (c) $i_{dj} dM_d/dt$ and $i_{qj} dM_q/dt$. (d) $\omega_e M_d i_{dj}$ and $-\omega_e M_q i_{qj}$. (e) $d\psi_{di}/dt$ and $d\psi_{qi}/dt$. (f) $\omega_e \psi_{di}$ and $-\omega_e \psi_{qi}$.

D. CURRENT-HARMONIC PREDICTION ERROR OF THE SIMPLIFIED MODEL

To determine how the induced-voltage harmonics identified above propagate into the current response, define

$$\eta_{dx} = v_{dx} - R_s i_{dx} - e_{dx}, \qquad \eta_{qx} = v_{qx} - R_s i_{qx} - e_{qx}. \tag{24}$$

where $x \in \{i, j\}$ denotes the winding-set index.

Applying (14) to both winding sets and substituting the definitions in (24) yield the coupled current dynamics:

$$\begin{pmatrix}\eta_{di} & \eta_{dj}\end{pmatrix}^T = \begin{pmatrix} L_{di} & M_d \\ M_d & L_{dj} \end{pmatrix} \begin{pmatrix} \frac{di_{di}}{dt} & \frac{di_{dj}}{dt} \end{pmatrix}^T, \tag{25}$$

and

$$\begin{pmatrix}\eta_{qi} & \eta_{qj}\end{pmatrix}^T = \begin{pmatrix} L_{qi} & M_q \\ M_q & L_{qj} \end{pmatrix} \begin{pmatrix} \frac{di_{qi}}{dt} & \frac{di_{qj}}{dt} \end{pmatrix}^T. \tag{26}$$

Solving for the current derivatives of winding set i gives

$$\frac{di_{di}}{dt} = \frac{L_{dj}\eta_{di} - M_d \eta_{dj}}{L_{di}L_{dj} - M_d^2}, \qquad \frac{di_{qi}}{dt} = \frac{L_{qj}\eta_{qi} - M_q \eta_{qj}}{L_{qi}L_{qj} - M_q^2}. \tag{27}$$

The corresponding expressions for winding set j are obtained by interchanging i and j. Equation (27) describes how the induced-voltage harmonics originating from the spatial harmonics give rise to harmonic current responses. The induced-voltage harmonics act as the harmonic excitation, while the inter-set mutual inductance modifies the resulting current response through the coupling between the two winding sets.

Combined with the induced-voltage components identified in Fig. 5, (27) explains the dominant current harmonics predicted by the detailed model. In particular, the sixth-order induced-voltage components excite sixth-order dq-current harmonics. Through the inverse coordinate transformation, these synchronous-frame components appear as fifth- and seventh-order phase-current harmonics. More generally, $6k$-order synchronous-frame harmonics correspond to the $6k-1$- and $6k+1$-order phase-domain harmonics.

Based on this analytical relationship, the simplified and detailed models were evaluated under identical control and operating conditions to verify the predicted harmonic current responses. The control structure shown in Fig. 6 and the parameters listed in Table 2 were used for both models. The switching and sampling frequencies were 10 kHz and 20 kHz, respectively, and the current-control bandwidth was 500 Hz.

Fig. 7 compares the predicted d- and q-axis currents, phase-a_1 current, and electromagnetic torque at 12.5 A_{rms} and $\beta = 15.7°$. The detailed model predicts pronounced sixth-order dq-current harmonics and the corresponding

TABLE 2. Controller parameters for two individual current control.

Parameter	Symbol	Design Expression	Value
Current-control bandwidth	f_{cc}	$f_{sw}/20$	500 Hz
d-axis proportional gain	$K_{p,d}$	$L_{d1}^0\omega_{cc}$	2.24
q-axis proportional gain	$K_{p,q}$	$L_{q1}^0\omega_{cc}$	4.45
d,q-axis integral gain	$K_{i,d}, K_{i,q}$	$R_s\omega_{cc}$	182.2

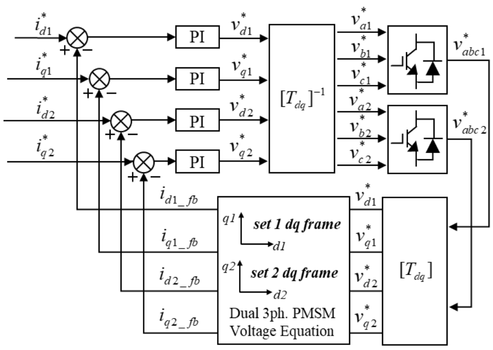

FIGURE 6. Two individual current-control structure used to compare the simplified and detailed models.

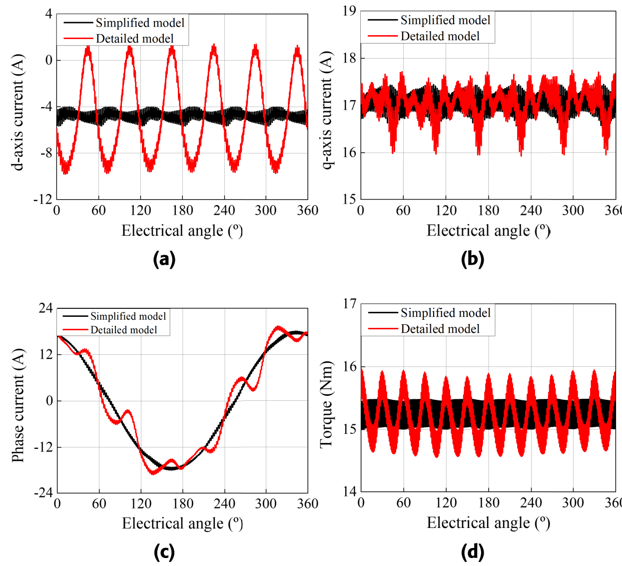

FIGURE 7. Predictions of the simplified and detailed models under two individual current control at 12.5 A_{rms} and $\beta = 15.7°$. (a) d-axis current. (b) q-axis current. (c) Phase-a_1 current. (d) Electromagnetic torque.

TABLE 3. Dominant current harmonics predicted by the simplified and detailed models.

Model	i_{a1} 5th	i_{a1} 7th	i_d 6th	i_q 6th
Simplified	0.11	0.11	0.21	0.07
Detailed	2.53	2.48	4.99	0.20

Current amplitudes are given in amperes.

fifth- and seventh-order phase-current harmonics, whereas these components are largely absent in the simplified model due to the omission of the spatial-harmonic-induced voltage components. As summarized in Table 3, the fifth- and seventh-order phase-current amplitudes are 2.53 and 2.48 A in the detailed model, compared with 0.11 A for both in the simplified model, while the sixth-order d-axis current increases from 0.21 to 4.99 A. These results confirm that the spatial-harmonic-induced voltage components are essential for accurately predicting the dominant current harmonics under two individual current control. Although Fig. 7(d) shows a difference in torque ripple, the fifth- and seventh-order current harmonics do not produce a net sixth-order torque ripple because of the 30° electrical displacement between the two winding sets. The remaining torque-ripple difference is mainly attributed to the twelfth-order component associated with the 11th- and 13th-order current harmonics, which is beyond the primary harmonic components considered in this study.

IV. HARMONIC-VOLTAGE-DEMAND PREDICTION ERRORS UNDER VSD CURRENT CONTROL

This section identifies the spatial-harmonic voltage sources omitted by the simplified model and explains how their omission causes harmonic-voltage-demand prediction errors under VSD current control.

A. VSD TRANSFORMATION, HARMONIC SEPARATION, AND VOLTAGE EQUATION

Under VSD current control, the six phase variables are decomposed into the torque-producing DQ subspace and the harmonic $DZQZ$ subspace as

$$\mathbf{x}_{\mathrm{VSD}} = \mathbf{T}_{\mathrm{VSD}}(\theta)\mathbf{x}_{abc,12}, \tag{28}$$

where

$$\begin{aligned} \mathbf{x}_{\mathrm{VSD}} &= \left(x_D \; x_Q \; x_{\mathrm{DZ}} \; x_{\mathrm{QZ}}\right)^T, \\ \mathbf{x}_{abc,12} &= \left(x_{a1} \; x_{b1} \; x_{c1} \; x_{a2} \; x_{b2} \; x_{c2}\right)^T. \end{aligned} \tag{29}$$

Here, θ denotes the electrical rotor position. The amplitude-invariant transformation matrix is provided in the Appendix. The zero-sequence components are excluded because the two winding sets have isolated neutral points.

For the 30° winding-set displacement, the VSD transformation separates the synchronous-frame harmonics as derived in the Appendix:

$$\begin{aligned} DQ: &\quad 0,\ 12k, &\quad k = 1, 2, 3, \ldots, \\ DZQZ: &\quad 6\ell, &\quad \ell = 1, 3, 5, \ldots. \end{aligned} \tag{30}$$

The corresponding flux linkages are

$$\begin{aligned} \lambda_D &= L_D i_D + \psi_D, &\quad \lambda_Q &= L_Q i_Q + \psi_Q, \\ \lambda_{\mathrm{DZ}} &= L_{\mathrm{DZ}} i_{\mathrm{DZ}} + \psi_{\mathrm{DZ}}, &\quad \lambda_{\mathrm{QZ}} &= L_{\mathrm{QZ}} i_{\mathrm{QZ}} + \psi_{\mathrm{QZ}}. \end{aligned} \tag{31}$$

Excluding the coupling between the DQ and $DZQZ$ subspaces introduced in Subsection IV-C, the voltage equations are

$$\begin{pmatrix} v_D \\ v_Q \end{pmatrix} = R_s \begin{pmatrix} i_D \\ i_Q \end{pmatrix} + \frac{d}{dt}\begin{pmatrix} \lambda_D \\ \lambda_Q \end{pmatrix} + \omega_e \begin{pmatrix} -\lambda_Q \\ \lambda_D \end{pmatrix}, \tag{32}$$

and

$$\begin{pmatrix} v_{\mathrm{DZ}} \\ v_{\mathrm{QZ}} \end{pmatrix} = R_s \begin{pmatrix} i_{\mathrm{DZ}} \\ i_{\mathrm{QZ}} \end{pmatrix} + \frac{d}{dt}\begin{pmatrix} \lambda_{\mathrm{DZ}} \\ \lambda_{\mathrm{QZ}} \end{pmatrix} + \omega_e \begin{pmatrix} -\lambda_{\mathrm{QZ}} \\ \lambda_{\mathrm{DZ}} \end{pmatrix}. \tag{33}$$

B. SIMPLIFIED MODEL

The simplified VSD model retains only the rotor-position-averaged FEA parameters in (21), thereby preserving the operating-point-dependent saturation and average inter-set coupling while excluding spatial harmonics.

Applying the VSD transformation to the zeroth-order inductance components gives

$$\begin{aligned} L_D^0 &= L_d^0 + M_d^0, \quad L_Q^0 = L_q^0 + M_q^0, \\ L_{\mathrm{DZ}}^0 &= L_d^0 - M_d^0, \quad L_{\mathrm{QZ}}^0 = L_q^0 - M_q^0. \end{aligned} \tag{34}$$

Similarly, the zeroth-order PM flux-linkage components are transformed as

$$\begin{aligned} \psi_D^0 &= \psi_d^0, \quad \psi_Q^0 = \psi_q^0, \\ \psi_{\mathrm{DZ}}^0 &= 0, \quad \psi_{\mathrm{QZ}}^0 = 0. \end{aligned} \tag{35}$$

Consequently, the simplified model neglects the rotor-position-dependent inductance and PM flux-linkage components and their associated nonfundamental voltages.

C. SPATIAL-HARMONIC VOLTAGE SOURCES RETAINED IN THE DETAILED MODEL

The detailed model retains the rotor-position-dependent parameter harmonics in (21). Applying the harmonic separation in (30) gives

$$\begin{aligned} L_D(\theta) &= L_d^0 + M_d^0 + L_{d,12k}(\theta) + M_{d,12k}(\theta), \\ L_Q(\theta) &= L_q^0 + M_q^0 + L_{q,12k}(\theta) + M_{q,12k}(\theta), \\ L_{\mathrm{DZ}}(\theta) &= L_d^0 - M_d^0 + L_{d,12k}(\theta) - M_{d,12k}(\theta), \\ L_{\mathrm{QZ}}(\theta) &= L_q^0 - M_q^0 + L_{q,12k}(\theta) - M_{q,12k}(\theta). \end{aligned} \tag{36}$$

where $L_{\mu,12k}(\theta)$ and $M_{\mu,12k}(\theta)$, with $\mu \in \{d, q\}$, denote the sums of the corresponding $12k$-order components.

The PM flux-linkage components are similarly obtained as

$$\begin{aligned} \psi_D(\theta) &= \psi_d^0 + \psi_{d,12k}(\theta), \quad \psi_Q(\theta) = \psi_q^0 + \psi_{q,12k}(\theta), \\ \psi_{\mathrm{DZ}}(\theta) &= \psi_{d,6\ell}(\theta), \quad \psi_{\mathrm{QZ}}(\theta) = \psi_{q,6\ell}(\theta). \end{aligned} \tag{37}$$

where $\psi_{\mu,12k}(\theta)$ and $\psi_{\mu,6\ell}(\theta)$ denote the sums of the corresponding harmonic components. The 6ℓ-order PM flux-linkage components in the *DZQZ* subspace therefore generate the associated nonfundamental voltage components.

The 6ℓ-order self-inductance components appear as cross-subspace coupling terms:

$$\begin{aligned} L_{\mathrm{DZ},D}(\theta) &= \sum_{\ell=1,3,5,\ldots} L_d^{6\ell} \sin\left(6\ell\theta + \alpha_{L,d}^{6\ell}\right), \\ L_{\mathrm{QZ},Q}(\theta) &= \sum_{\ell=1,3,5,\ldots} L_q^{6\ell} \sin\left(6\ell\theta + \alpha_{L,q}^{6\ell}\right). \end{aligned} \tag{38}$$

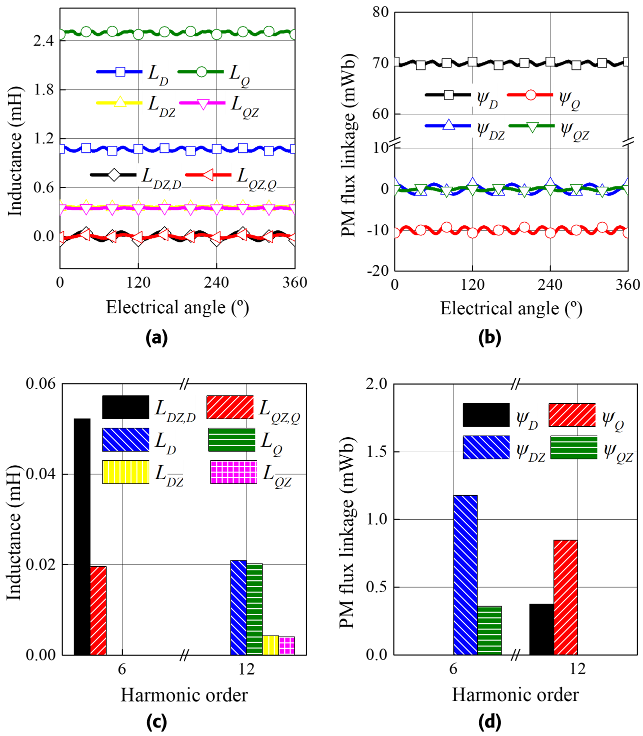

FIGURE 8. Rotor-position-dependent parameters in the VSD reference frame. (a) Inductance waveforms. (b) PM flux-linkage waveforms. (c) Inductance harmonic spectra. (d) PM flux-linkage harmonic spectra.

The first and second subscripts denote the flux-linkage and current axes, respectively, and the reverse coupling terms are identical by inductance reciprocity.

Fig. 8 shows the transformed parameters and their harmonic spectra. The inductances L_D, L_Q, L_{DZ}, and L_{QZ} contain dominant 12th-order components, whereas $L_{\mathrm{DZ},D}$ and $L_{\mathrm{QZ},Q}$ contain dominant sixth-order components. Similarly, the PM flux linkages contain dominant 12th-order components in the *DQ* subspace and sixth-order components in the *DZQZ* subspace.

The coupling inductances in (38) generate additional *DZQZ* voltages from the *DQ* currents:

$$\begin{pmatrix} v_{\mathrm{DZ}}^c \\ v_{\mathrm{QZ}}^c \end{pmatrix} = \frac{d}{dt}\begin{pmatrix} L_{\mathrm{DZ},D}\, i_D \\ L_{\mathrm{QZ},Q}\, i_Q \end{pmatrix} + \omega_e \begin{pmatrix} -L_{\mathrm{QZ},Q}\, i_Q \\ L_{\mathrm{DZ},D}\, i_D \end{pmatrix}. \tag{39}$$

Because these coupling inductances contain 6ℓ-order components, both terms in (39) generate 6ℓ-order *DZQZ* voltages.

The total *DZQZ* voltages of the detailed model are

$$\begin{pmatrix} v_{\mathrm{DZ}}^{\det} \\ v_{\mathrm{QZ}}^{\det} \end{pmatrix} = \begin{pmatrix} v_{\mathrm{DZ}} \\ v_{\mathrm{QZ}} \end{pmatrix} + \begin{pmatrix} v_{\mathrm{DZ}}^c \\ v_{\mathrm{QZ}}^c \end{pmatrix}, \tag{40}$$

where v_{DZ} and v_{QZ} are defined in (33).

Therefore, the detailed model retains two principal 6ℓ-order *DZQZ* voltage sources: the PM flux-linkage harmonics in (37) and the cross-subspace coupling voltages in (39). For the considered machine, the sixth-order components are dominant. Both sources are removed by parameter averaging.

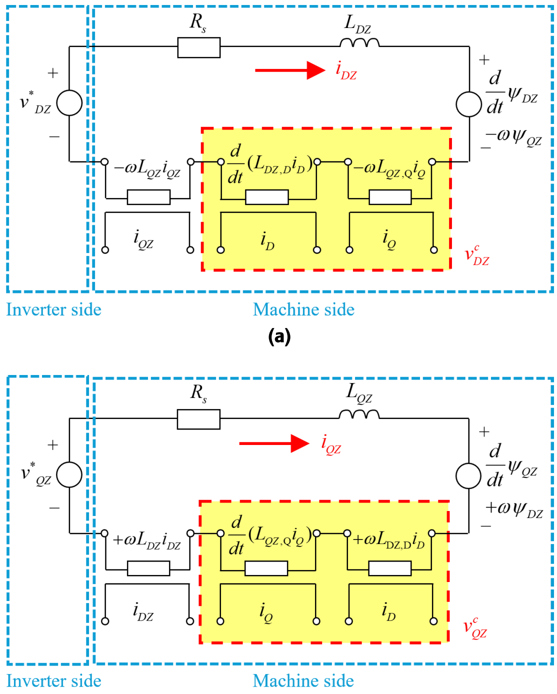

FIGURE 9. **Equivalent circuits of the harmonic subspace including the coupling voltages between the *DQ* and *DZQZ* subspaces. (a) *DZ*-axis equivalent circuit. (b) *QZ*-axis equivalent circuit.**

D. HARMONIC-VOLTAGE-DEMAND PREDICTION ERROR OF THE SIMPLIFIED MODEL

Fig. 9 shows the *DZ*- and *QZ*-axis equivalent circuits including the PM-induced and cross-subspace coupling voltages identified above.

The PM-induced voltage is

$$\begin{pmatrix} e_{\mathrm{DZ}} \\ e_{\mathrm{QZ}} \end{pmatrix} = \frac{d}{dt}\begin{pmatrix} \psi_{\mathrm{DZ}} \\ \psi_{\mathrm{QZ}} \end{pmatrix} + \omega_e \begin{pmatrix} -\psi_{\mathrm{QZ}} \\ \psi_{\mathrm{DZ}} \end{pmatrix}. \tag{41}$$

Under VSD current control, the resonant controllers suppress the sixth-order *DZQZ* currents. For the following analytical approximation, the sixth-order residual currents and their resistive and inductive voltage drops are assumed to be small, and inverter nonlinearities, such as dead time and semiconductor voltage drops, are neglected relative to the motor-side harmonic voltage sources. Accordingly, the required sixth-order voltage command is approximated as

$$\begin{pmatrix} v^{*,\mathrm{det}}_{\mathrm{DZ},6} \\ v^{*,\mathrm{det}}_{\mathrm{QZ},6} \end{pmatrix} \approx \begin{pmatrix} e_{\mathrm{DZ},6} \\ e_{\mathrm{QZ},6} \end{pmatrix} + \begin{pmatrix} v^{c}_{\mathrm{DZ},6} \\ v^{c}_{\mathrm{QZ},6} \end{pmatrix}, \tag{42}$$

where the superscript $*$ denotes the controller voltage command and the subscript 6 denotes the sixth-order synchronous-frame component.

Because the simplified model does not retain the sixth-order spatial-harmonic voltage sources, the predicted sixth-order *DZQZ* voltage demand is negligible.

The sixth-order synchronous-frame components correspond to the fifth- and seventh-order phase-domain components. Under two individual current control, the omitted spatial harmonics primarily result in current-harmonic prediction errors, whereas under VSD current control, active suppression of the corresponding *DZQZ* currents shifts their effect to the controller-voltage demand.

To evaluate this effect, the simplified and detailed models were implemented under identical control and operating conditions using the VSD control structure in Fig. 10 and the parameters in Table 4. The switching and sampling frequencies were 10 kHz and 20 kHz, respectively, and the current-control bandwidth was 500 Hz. The proportional–resonant controllers in the *DZQZ* subspace were tuned to the sixth-order synchronous-frame component as

$$\omega_r = 6\omega_e. \tag{43}$$

Fig. 11 compares the predicted *DZ*- and *QZ*-axis voltage commands, phase-a_1 voltage, and electromagnetic torque at 12.5 $\mathrm{A_{rms}}$ and $\beta = 15.7°$. The detailed model predicts pronounced harmonic voltage commands required to suppress the spatial-harmonic-induced currents, whereas the simplified model substantially underestimates this voltage demand and the resulting phase-voltage distortion.

As summarized in Table 5, the sixth-order *DZ*-axis voltage increases from 0.07 V in the simplified model to 2.81 V in the detailed model, while the seventh-order phase-voltage component increases from 0.12 to 1.66 V. These results confirm that neglecting the spatial harmonics leads to substantial underestimation of the harmonic voltage demand under VSD current control. The torque-ripple difference between the two models is governed primarily by higher-order current harmonics, as discussed in Section III-D.

TABLE 4. **Controller parameters for VSD current control.**

Parameter	Symbol	Design Expression	Value
Current-control bandwidth	f_{cc}	$f_{\mathrm{sw}}/20$	500 Hz
D-axis proportional gain	$K_{p,D}$	$L_D^0\omega_{\mathrm{cc}}$	3.20
Q-axis proportional gain	$K_{p,Q}$	$L_Q^0\omega_{\mathrm{cc}}$	7.41
DZ-axis proportional gain	$K_{p,\mathrm{DZ}}$	$L_{\mathrm{DZ}}^0\omega_{\mathrm{cc}}$	1.62
QZ-axis proportional gain	$K_{p,\mathrm{QZ}}$	$L_{\mathrm{QZ}}^0\omega_{\mathrm{cc}}$	1.21
D,*Q*-axis integral gain	$K_{i,D}$,$K_{i,Q}$	$R_s\omega_{\mathrm{cc}}$	182.21
DZ,*QZ*-axis resonant gain	$K_{r,\mathrm{DZ}}$,$K_{r,\mathrm{QZ}}$	$5R_s\omega_{\mathrm{cc}}$	911.06

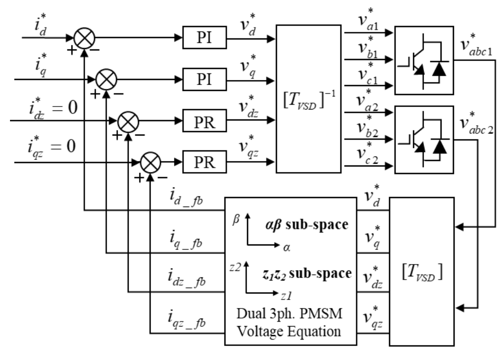

FIGURE 10. **VSD current-control structure used to compare the simplified and detailed models.**

TABLE 5. Dominant voltage harmonics predicted by the simplified and detailed models.

Model	v_{a1}^*	v_{a1}^*	v_{DZ}^*	v_{QZ}^*
	5th	7th	6th	6th
Simplified	0.31	0.12	0.07	0.19
Detailed	0.42	1.66	2.81	0.40

Voltage amplitudes are given in volts.

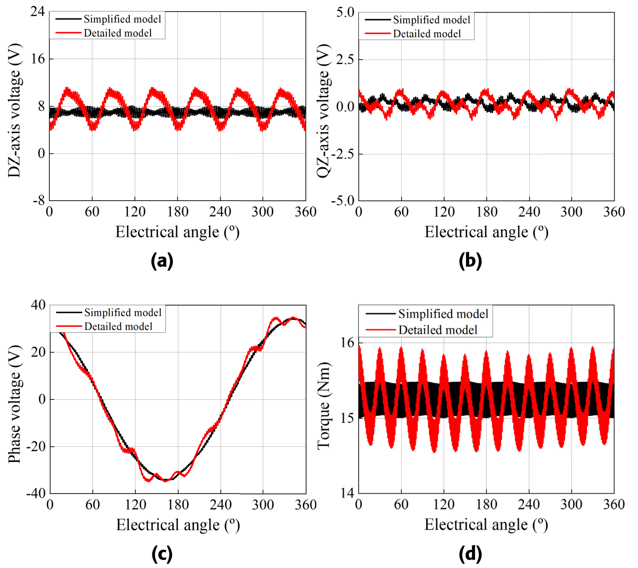

FIGURE 11. Predictions of the simplified and detailed models under VSD current control at 12.5 A_{rms} and $\beta = 15.7°$. (a) DZ-axis voltage command. (b) QZ-axis voltage command. (c) Phase-a_1 voltage. (d) Electromagnetic torque.

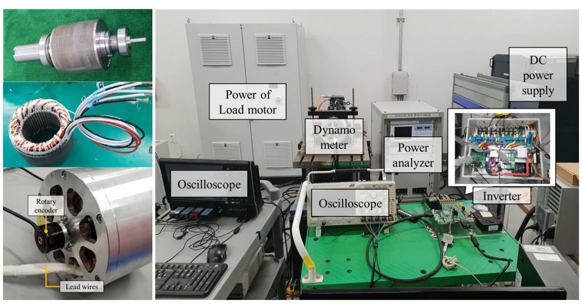

FIGURE 12. Fabricated prototype motor and experimental setup for the dual three-phase PMSM drive test.

V. EXPERIMENTAL VALIDATION

This section experimentally validates the control-dependent prediction characteristics of the simplified and detailed models analyzed in Sections III and IV.

Fig. 12 shows the fabricated 8-pole/48-slot asymmetrical dual three-phase IPMSM and the experimental setup. The test bench includes a 200-V dc-link supply, a six-phase inverter, a LeCroy HDO4054A oscilloscope with CP150B current probes, and a 5-kW dynamometer. The switching and controller sampling frequencies were 10 and 20 kHz, respectively, and the inverter current limit was 30 A. The inverter operated without voltage saturation over the tested range, and no semiconductor voltage-drop compensation was applied. Phase currents and line-to-line voltages were measured using the current probes and oscilloscope, respectively, with a sampling interval of 2×10^{-7} s.

TABLE 6. Experimental operating points for the current-phase-angle and speed-variation tests.

Point	Speed (r/min)	Current Magnitude (A_{rms})	Current Phase Angle (°)
1	1000	10.0	0.0
2	1000	10.0	30.0
3	1000	10.0	60.0
4	500	12.5	15.7
5	1000	12.5	15.7
6	2000	12.5	15.7

The six operating points are listed in Table 6. Points 1–3 correspond to current-phase-angle variation at 1000 r/min and 10 A_{rms}, with $\beta = 0°$, 30°, and 60°, whereas Points 4–6 correspond to speed variation at 12.5 A_{rms} and $\beta = 15.7°$, at 500, 1000, and 2000 r/min. Both models use identical inverter, controller, and operating conditions, such that their prediction differences arise only from the treatment of rotor-position-dependent spatial harmonics. The experimental validation covers current-phase-angle and speed variations within the tested range; voltage-limited field-weakening operation was not included in the present experiments.

A. CURRENT-HARMONIC VALIDATION UNDER TWO INDIVIDUAL CURRENT CONTROL

Figs. 13 and 14 compare the predicted and measured phase-current waveforms and harmonic spectra for the current phase angle- and speed-variation tests, respectively. Across all six operating points, the detailed model predicts fifth- and seventh-order current harmonics comparable to the measured values, whereas these components are nearly absent in the simplified model.

In Fig. 13, both the detailed-model and measured results show a pronounced increase in the seventh-order current harmonic with increasing current phase angle. Fig. 14 also shows comparable fifth- and seventh-order harmonic amplitudes between the detailed model and measurements over the tested speed range. These results validate the analysis in Section III and confirm that neglecting the spatial-harmonic-induced voltage components leads to substantial underestimation of the current harmonics under two individual current control.

The quantitative prediction accuracy based on the mean absolute percentage error (MAPE) is summarized in Table 7. For the fifth- and seventh-order current harmonics over all six operating points, the MAPEs decrease from 99.8% and 99.6% with the simplified model to 21.3% and 23.3% with the detailed model, respectively. These results quantitatively confirm that retaining the spatial-harmonic-induced voltage components substantially improves the prediction of the dominant current harmonics under two individual current control.

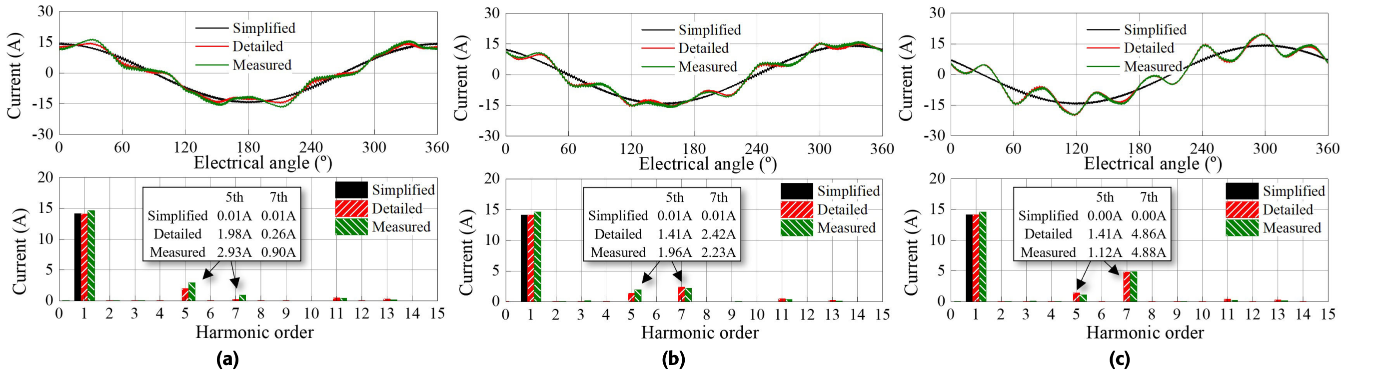

FIGURE 13. **Comparison of the phase currents predicted by the simplified and detailed models with the measured currents under two individual current control for the current-phase-angle-variation test at 1000 r/min and 10 A_{rms}: (a) $\beta = 0°$, (b) $\beta = 30°$, and (c) $\beta = 60°$.**

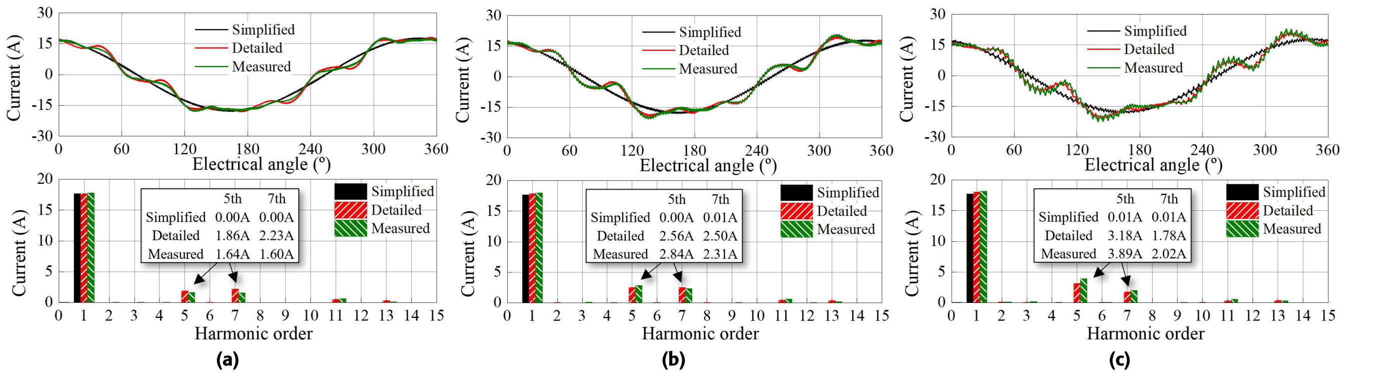

FIGURE 14. **Comparison of the phase currents predicted by the simplified and detailed models with the measured currents under two individual current control for the speed-variation test at 12.5 A_{rms} and $\beta = 15.7°$: (a) 500 r/min, (b) 1000 r/min, and (c) 2000 r/min.**

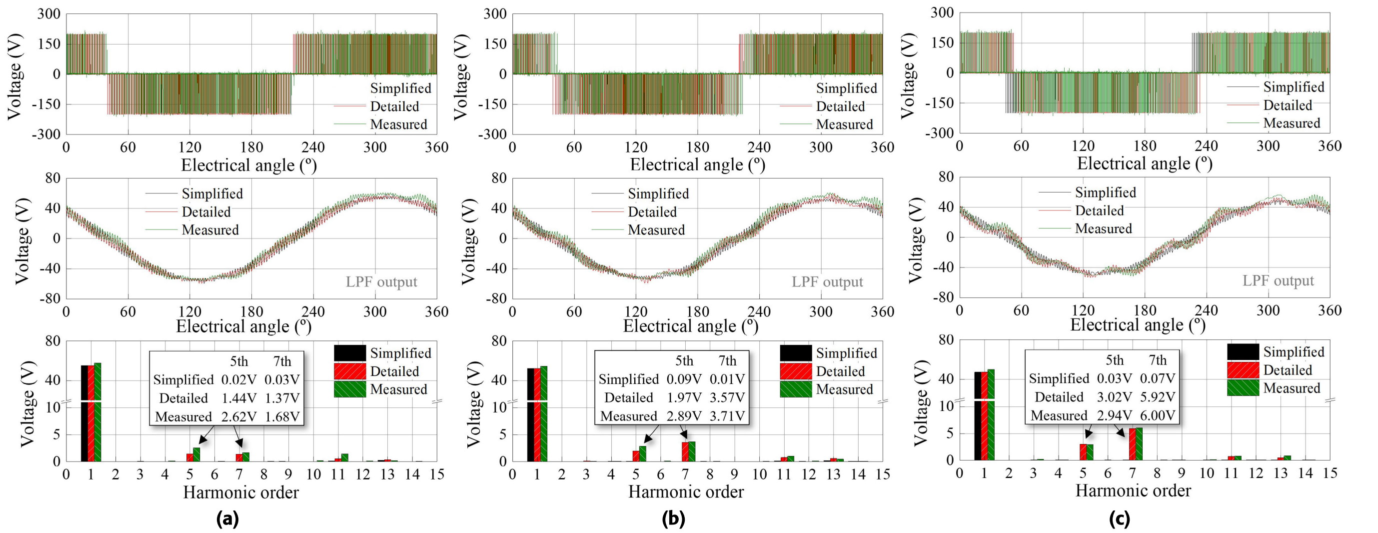

FIGURE 15. **Comparison of the voltage waveforms predicted by the simplified and detailed models with the measured voltages under VSD current control for the current-phase-angle-variation test at 1000 r/min and 10 A_{rms}: (a) $\beta = 0°$, (b) $\beta = 30°$, and (c) $\beta = 60°$.**

B. HARMONIC-VOLTAGE-DEMAND VALIDATION UNDER VSD CURRENT CONTROL

Figs. 15 and 16 compare the predicted and measured line-to-line voltages for the current phase angle- and speed-variation tests, respectively. The fifth- and seventh-order harmonic amplitudes were extracted from the FFT of the raw voltage waveforms. The LPF outputs were used only to visually compare the low-order harmonic voltage behavior and the agreement between the measured and predicted waveforms.

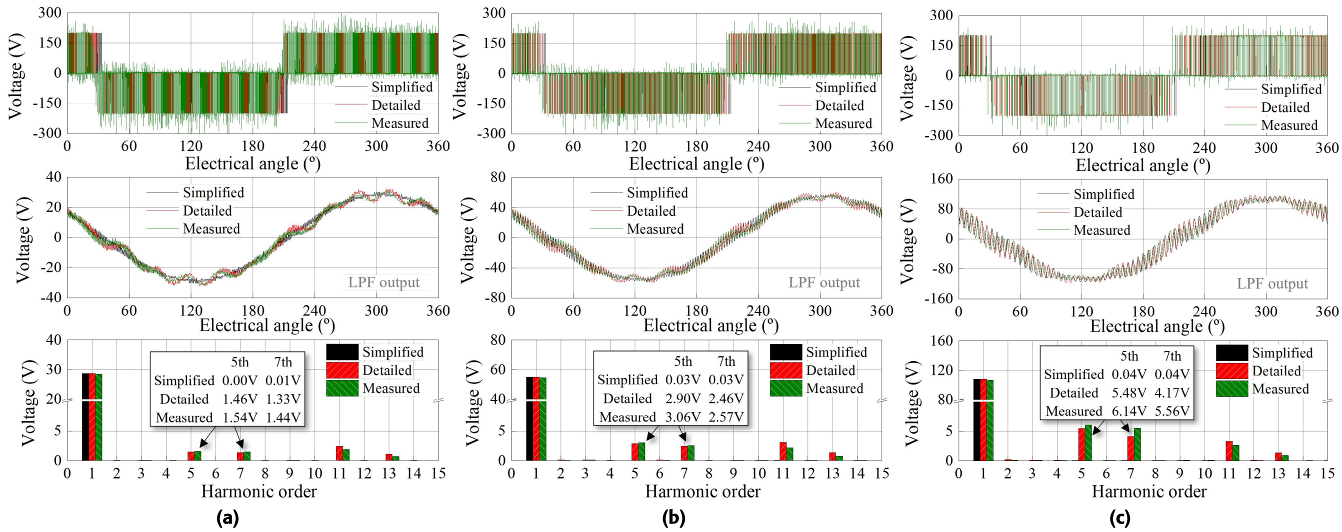

FIGURE 16. Comparison of the voltage waveforms predicted by the simplified and detailed models with the measured voltages under VSD current control for the speed-variation test at 12.5 A_{rms} and $\beta = 15.7°$: (a) 500 r/min, (b) 1000 r/min, and (c) 2000 r/min.

TABLE 7. Mean absolute percentage errors of the dominant harmonic predictions.

Model	i_{a1} 5th	i_{a1} 7th	v_{a1b1} 5th	v_{a1b1} 7th
Simplified	99.8	99.6	82.9	83.6
Detailed	21.3	23.3	16.8	10.1

Across all six operating points, the detailed model reproduces the measured fifth- and seventh-order voltage harmonics and their variations, whereas the simplified model substantially underestimates them. As summarized in Table 7, the corresponding MAPEs decrease from 82.9% and 83.6% to 16.8% and 10.1%, respectively, confirming the importance of the spatial-harmonic voltage sources for harmonic-voltage-demand prediction. The remaining discrepancies may arise from measurement uncertainty, finite FFT resolution, and unmodeled inverter nonlinearities such as dead time and semiconductor voltage drops; the present study instead focuses on prediction errors caused by spatial-harmonic omission.

VI. CONCLUSION

This paper analyzed the effects of rotor-position-dependent spatial harmonics on current and voltage prediction in dual three-phase PMSMs under two current-control strategies. The simplified and detailed models were constructed from identical FEA-based parameters, with both retaining the same operating-point-dependent magnetic-saturation state and average inter-set coupling, while only the detailed model retained the spatial harmonics.

Under two individual current control, the omitted parameter-derivative and speed-induced harmonic voltage components excite sixth-order *dq*-current harmonics, which appear as fifth- and seventh-order phase-current harmonics. Under VSD current control, these harmonic currents are actively suppressed in the *DZQZ* subspace, and the omitted spatial harmonics instead appear primarily as harmonic voltage demand through the *DZQZ* PM-induced voltages and the cross-subspace inductive coupling. Consequently, the simplified model underestimates the dominant current harmonics under two individual current control and the harmonic voltage demand under VSD current control.

Current phase angle- and speed-variation experiments at six operating points confirmed these control-dependent prediction characteristics. The detailed model reproduced the measured fifth- and seventh-order current and voltage harmonics and their variations with current phase angle and speed, whereas the simplified model predicted only negligible low-order harmonics. These results demonstrate that the validity of a rotor-position-averaged machine model depends on the applied current-control strategy and the quantity to be predicted.

APPENDIX
COORDINATE TRANSFORMATIONS AND HARMONIC-ORDER SEPARATION

The transformation matrix for two individual current control is

$$\mathbf{T}_P(\theta) = \begin{pmatrix} \mathbf{T}_1(\theta) & \mathbf{0}_{2\times 3} \\ \mathbf{0}_{2\times 3} & \mathbf{T}_2(\theta) \end{pmatrix}, \tag{44}$$

where

$$\mathbf{T}_1(\theta) = \frac{2}{3}\begin{pmatrix} \cos\theta & \cos\left(\theta - \frac{2\pi}{3}\right) & \cos\left(\theta + \frac{2\pi}{3}\right) \\ -\sin\theta & -\sin\left(\theta - \frac{2\pi}{3}\right) & -\sin\left(\theta + \frac{2\pi}{3}\right) \end{pmatrix}, \tag{45}$$

and

$$\mathbf{T}_2(\theta) = \mathbf{T}_1\left(\theta - \frac{\pi}{6}\right). \tag{46}$$

The factor 2/3 provides amplitude-invariant scaling, and the angular shift accounts for the 30° displacement between the winding sets.

The amplitude-invariant VSD transformation is

$$\mathbf{T}_{\mathrm{VSD}}(\theta) = \frac{1}{2}\begin{pmatrix} \mathbf{T}_1(\theta) & \mathbf{T}_2(\theta) \\ \mathbf{T}_1(\theta) & -\mathbf{T}_2(\theta) \end{pmatrix}, \tag{47}$$

where the upper and lower block rows correspond to the *DQ* and *DZQZ* subspaces, respectively.

To derive the corresponding harmonic-order separation, let $\delta = -\pi/6$ denote the winding-set displacement. For a $6r$-order synchronous-frame component,

$$x_{\mu 2}^{6r}(\theta) = x_{\mu 1}^{6r}(\theta + \delta) = (-1)^r x_{\mu 1}^{6r}(\theta), \qquad \mu \in \{d, q\}, \tag{48}$$

because $6r\delta = -r\pi$.

The VSD transformation forms the common and differential components as

$$x_{\mu,\mathrm{com}}^{6r} = \frac{x_{\mu 1}^{6r} + x_{\mu 2}^{6r}}{2}, \quad x_{\mu,\mathrm{dif}}^{6r} = \frac{x_{\mu 1}^{6r} - x_{\mu 2}^{6r}}{2}. \tag{49}$$

Hence, even and odd values of r appear in the *DQ* and *DZQZ* subspaces, respectively:

$$\begin{aligned} DQ: &\quad 0,\ 12k, \quad k = 1, 2, 3, \ldots, \\ DZQZ: &\quad 6\ell, \quad\quad \ell = 1, 3, 5, \ldots. \end{aligned} \tag{50}$$

REFERENCES

[1] E. Levi, R. Bojoi, F. Profumo, H. A. Toliyat, and S. Williamson, "Multiphase induction motor drives—A technology status review," *IET Electric Power Appl.*, vol. 1, no. 4, pp. 489–516, Jul. 2007.

[2] B. Tian, G. Mirzaeva, Q.-T. An, L. Sun, and D. Semenov, "Fault-tolerant control of a five-phase permanent magnet synchronous motor for industry applications," *IEEE Trans. Ind. Appl.*, vol. 54, no. 4, pp. 3943–3952, Jul. 2018.

[3] A. Salem and M. Narimani, "A review on multiphase drives for automotive traction applications," *IEEE Trans. Transport. Electrific.*, vol. 5, no. 4, pp. 1329–1348, Dec. 2019.

[4] I. Subotic, N. Bodo, E. Levi, M. Jones, and V. Levi, "Isolated chargers for EVs incorporating six-phase machines," *IEEE Trans. Ind. Electron.*, vol. 63, no. 1, pp. 653–664, Jan. 2016.

[5] V. I. Patel, J. Wang, W. Wang, and X. Chen, "Six-phase fractional-slot-per-pole-per-phase permanent-magnet machines with low space harmonics for electric vehicle application," *IEEE Trans. Ind. Appl.*, vol. 50, no. 4, pp. 2554–2563, Jul. 2014.

[6] S. Williamson and S. Smith, "Pulsating torque and losses in multiphase induction machines," in *Proc. IEEE Ind. Appl. Conf. 36th IAS Annu. Meeting*, vol. 2, Jul. 2001, pp. 1155–1162.

[7] C. Zeng, Y. Chen, K. Liu, C. Miao, Z. Zhao, Y. Ding, H. Cai, and J. Chen, "Torque optimization of a dual three-phase permanent magnet synchronous machine with asymmetric rotor core for electric vehicles," in *Proc. 26th Int. Conf. Electr. Mach. Syst. (ICEMS)*, Nov. 2023, pp. 2612–2617.

[8] Y. Hu, Z.-Q. Zhu, and K. Liu, "Current control for dual three-phase permanent magnet synchronous motors accounting for current unbalance and harmonics," *IEEE J. Emerg. Sel. Topics Power Electron.*, vol. 2, no. 2, pp. 272–284, Jun. 2014.

[9] Y. Hu, Z. Q. Zhu, and M. Odavic, "Comparison of two-individual current control and vector space decomposition control for dual three-phase PMSM," *IEEE Trans. Ind. Appl.*, vol. 53, no. 5, pp. 4483–4492, Sep. 2017.

[10] C. Zhou, G. Yang, and J. Su, "PWM strategy with minimum harmonic distortion for dual three-phase permanent-magnet synchronous motor drives operating in the overmodulation region," *IEEE Trans. Power Electron.*, vol. 31, no. 2, pp. 1367–1380, Feb. 2016.

[11] Y. Luo and C. Liu, "A simplified model predictive control for a dual three-phase PMSM with reduced harmonic currents," *IEEE Trans. Ind. Electron.*, vol. 65, no. 11, pp. 9079–9089, Nov. 2018.

[12] X. Chen, J. Wang, B. Sen, P. Lazari, and T. Sun, "A high-fidelity and computationally efficient model for interior permanent-magnet machines considering the magnetic saturation, spatial harmonics, and iron loss effect," *IEEE Trans. Ind. Electron.*, vol. 62, no. 7, pp. 4044–4055, Jul. 2015.

[13] J. Zou, C. Liu, Y. Xu, and G. Yu, "A high-precision model for dual three-phase PMSM considering the effect of harmonics, magnetic saturation, and electromagnetic coupling," *IEEE Trans. Transport. Electrific.*, vol. 10, no. 2, pp. 2456–2468, Jun. 2024.

[14] P. Hollstegge, D. Keller, and R. W. De Doncker, "Dual three-phase machine modeling and control including saturation, rotor position dependency and reduction of low current harmonics," in *Proc. 7th Int. Electric Drives Prod. Conf. (EDPC)*, Dec. 2017, pp. 1–9.

[15] S. Agoro and I. Husain, "High-fidelity nonlinear modeling of an asymmetrical dual three-phase PMSM," in *Proc. IEEE Int. Electric Mach. Drives Conf. (IEMDC)*, May 2023, pp. 1–7.

[16] S. Na, J. Choi, Y. Hwang, and J. Yoo, "Partially linearized flux model for fast high-fidelity simulation of dual three-phase PMSM drive," *IEEE Trans. Transport. Electrific.*, vol. 12, no. 3, pp. 4977–4987, Jun. 2026.

[17] Y.-N. Bae, J.-Y. Ryu, and M.-S. Lim, "Design-oriented prediction and reduction of voltage harmonics in dual three-phase PMSMs for improved voltage utilization," *IEEE Trans. Ind. Electron.*, early access, Jun. 23, 2026, doi: 10.1109/TIE.2026.3704772.

[18] T. Li, X. Sun, Z. Su, X. Zha, A. Dianov, V. Prakht, G. Demidova, and J. Ma, "Model-free predictive control for harmonic suppression of PMSMs based on adaptive resonant controller," *IEEE Trans. Energy Convers.*, vol. 40, no. 4, pp. 3104–3114, Dec. 2025.

[19] T. Li, X. Sun, M. Yao, D. Guo, and Y. Sun, "Improved finite control set model predictive current control for permanent magnet synchronous motor with sliding mode observer," *IEEE Trans. Transport. Electrific.*, vol. 10, no. 1, pp. 699–710, Mar. 2024.

YE-NA BAE received the bachelor's degree in automotive engineering from Kookmin University, Seoul, South Korea, in 2020. She is currently pursuing the Ph.D. degree in automotive engineering with Hanyang University, Seoul. Her research interests include optimization, design, and systems modeling of e-mobility.

HYUN-JEONG HONG received the bachelor's and master's degrees in automotive engineering from Hanyang University, Seoul, South Korea, in 2023 and 2025, respectively. Her research interests include design and analysis of electric motor systems.

JUN-YEOL RYU received the bachelor's degree in mechanical engineering and electronic systems engineering from Hanyang University, Ansan, South Korea, in 2016, and the Ph.D. degree in automotive engineering from Hanyang University, Seoul, South Korea, in 2023. Since 2023, he has been with Korea Automotive Technology Institute, Cheonan, South Korea, where he is currently a Senior Researcher. His research interests include design and optimization of electric machines and the analysis of electromagnetic fields.

MYUNG-HWAN YOON received the bachelor's degree in mechanical engineering and the master's and Ph.D. degrees in automotive engineering from Hanyang University, Seoul, South Korea, in 2011, 2013, and 2018, respectively. From 2018 to 2019, he was a Senior Research Engineer with Hyundai Motor Company, Hwaseong, South Korea. Since 2019, he has been a Principal Researcher with Korea Electronics Technology Institute. His research interests include electromagnetic field analysis and electric machinery for automotive applications.

MYUNG-SEOP LIM (Senior Member, IEEE) received the bachelor's degree in mechanical engineering and the master's and Ph.D. degrees in automotive engineering from Hanyang University, Seoul, South Korea, in 2012, 2014, and 2017, respectively. From 2017 to 2018, he was a Research Engineer with Hyundai Mobis, Yongin, South Korea. From 2018 to 2019, he was an Assistant Professor with Yeungnam University, Daegu, South Korea. Since 2019, he has been with Hanyang University, where he is currently an Assistant Professor.